

## Self-Limited Accretion onto Embedded Binaries in a Uniform Medium

MARCUS DUPONT <sup>1</sup> AND ELIOT QUATAERT <sup>1</sup>

<sup>1</sup>*Department of Astrophysical Sciences, Princeton University, Princeton, NJ, 08544, USA*

### ABSTRACT

We study accretion from a uniform gas at rest onto equal-mass binaries – the binary Bondi problem – as a function of adiabatic index  $\gamma$  and compactness  $\xi \equiv R_B/a$ , where  $R_B$  is the Bondi radius of the binary and  $a$  is the component separation. We present three-dimensional hydrodynamic simulations spanning  $\xi = \{0.1, 1, 10\}$  at  $\gamma = \{1, 4/3, 5/3\}$ . Isothermal gas ( $\gamma = 1$ ) accretes cooperatively at high compactness, with efficiency  $\eta \equiv \dot{M}_{\text{binary}}/\dot{M}_{\text{Bondi}} \rightarrow 1$  for  $\xi \gg 1$  and a stable sonic surface that screens the orbital modulation. Adiabatic gas ( $\gamma > 1$ ) is self-limiting: the orbit drives shocks that generate entropy, producing convective turbulence that suppresses accretion to  $\eta \approx 0.3$  ( $\gamma = 4/3$ ) and  $\eta \approx 0.1$  ( $\gamma = 5/3$ ), burying the orbital signature in broadband noise. We derive a stability criterion from first principles: the sonic surface is the separatrix of the Bondi saddle point, and the binary annihilates it in  $N \propto (\gamma - 1)^{-1}(\sqrt{\xi/\xi_m} - 1)$  orbits, where  $\xi_m = 4/(5 - 3\gamma)$  is the container threshold at which the sonic surface first encloses the binary, and the  $(\gamma - 1)^{-1}$  divergence follows from the lack of entropy generation at isothermal shocks. For  $\gamma = 5/3$ , no saddle point exists at any  $\xi$  and the neutrally stratified Bondi profile is convectively unstable by a distinct mechanism. The single comparison  $t_{\text{cool}}$  versus  $NT$  – where  $T$  is the orbital period – determines whether an embedded binary accretes cooperatively or throttles its own fuel supply; simulations confirm the analytic thresholds and scaling.

*Keywords:* Accretion (14) — Active Galactic Nuclei (16) — Hydrodynamical Simulations (767) — Supermassive Black Holes (1663)

### 1. INTRODUCTION

The simplest question about a binary embedded in a uniform gaseous medium is whether it accretes like a single object. For total mass  $M = m_1 + m_2$ , separation  $a$ , and ambient sound speed  $c_\infty$ , the answer depends on compactness  $\xi \equiv R_B/a$ , where  $R_B = GM/c_\infty^2$  is the Bondi radius (H. Bondi 1952). When  $\xi \ll 1$ , each component accretes independently. When  $\xi \gg 1$ , the binary is deeply embedded within a shared Bondi sphere and should accrete cooperatively with efficiency  $\eta \equiv \dot{M}_{\text{binary}}/\dot{M}_{\text{Bondi}} \rightarrow 1$ . We show that this expectation fails for any gas with  $\gamma > 1$ : the binary orbit drives shocks that generate entropy, producing convective turbulence that suppresses accretion and produces sufficient variability in the accretion to suppress the orbital signal.

The interaction of binaries with gas has been studied most extensively in the circumbinary disk geometry, where angular momentum produces a rotationally supported structure and the coupling is mediated by res-

onant and viscous torques (see e.g., P. Artymowicz & S. H. Lubow 1994, 1996; A. I. MacFadyen & M. Milosavljević 2008); see D. Lai & D. J. Muñoz (2023) for a review. The complementary regime – accretion from a uniform, pressure-supported medium at rest onto a binary potential – was first simulated by B. D. Farris et al. (2010), who performed general-relativistic calculations near coalescence and coined the term “binary Bondi.” This problem was also studied in more detail recently using general-relativistic MHD simulations by S. M. Ressler et al. (2025). In both works the focus was the electromagnetic counterpart to merger; at the wide separations relevant to most of a binary’s lifetime, the steady-state thermodynamic response was not addressed. In the supersonic wind limit, A. Antoni et al. (2019) measured binary Bondi–Hoyle–Lyttleton drag and accretion rates. In the subsonic limit, linear calculations for single (H. Kim & W.-T. Kim 2007; D. O’Neill et al. 2024) and binary (H. Kim et al. 2008) perturbers cannot access the entropy-driven instability we identify, because the linear density wake is independent of the equation of state. W.-T. Kim (2010) entered the nonlinear regime for a single perturber in  $\gamma = 5/3$  gas,

finding hydrostatic envelopes but no convective disruption – the quadrupolar forcing of a binary is required.

The binary Bondi problem applies across the electromagnetic and gravitational wave spectrum. Pulsar timing arrays have detected the nanohertz background from supermassive black hole (SMBH) binaries (G. Agazie et al. 2023; EPTA Collaboration et al. 2023; D. J. Reardon et al. 2023; H. Xu et al. 2023), and population synthesis models often adopt gas hardening prescriptions calibrated to laminar accretion (Z. Haiman et al. 2009; A. Sesana 2013; L. Z. Kelley et al. 2017). LISA (M. Colpi et al. 2024) will track individual inspiral waveforms through the regime where gas coupling shapes the orbit. At the stellar-mass end, LIGO–Virgo–KAGRA (LIGO Scientific Collaboration et al. 2015; F. Acernese et al. 2015; Kagra Collaboration et al. 2019) detects mergers whose progenitors may have formed in gaseous environments. Electromagnetic surveys searching for periodic binary active galactic nuclei (AGN) signatures have yielded almost uniformly null results: K. El-Badry et al. (2025) tested 181 Gaia DR3 candidates and found all were false positives. The binary Bondi flow provides a mechanism for suppressing periodic accretion signatures and reducing the effective accretion efficiency of binaries in adiabatic environments relative to laminar estimates.

In this work, we present three-dimensional inviscid hydrodynamic simulations spanning  $\xi = 0.1$ –10 at  $\gamma = 1$ ,  $4/3$ , and  $5/3$ , together with an analytic stability criterion that predicts the onset, timescale, and character of the entropy-driven turbulence. Section 2 derives the criterion. Section 3 describes the numerical setup. Section 4 presents results. Section 5 discusses implications. Section 6 summarizes.

## 2. THE STABILITY CRITERION

We work in units where  $G = \rho_\infty = a = 1$ . The mass ratio is  $q \equiv m_2/m_1 \leq 1$  where  $M = m_1 + m_2 = 1$ . Three dimensionless parameters characterize the problem: the compactness  $\xi \equiv GM/(c_\infty^2 a) = 1/c_\infty^2$ , the adiabatic index  $\gamma$ , and  $q$ . The accretion efficiency is

$$\eta(\xi, \gamma, q) \equiv \frac{\dot{M}_{\text{binary}}}{\dot{M}_{\text{Bondi}}(M)}, \quad (1)$$

where  $\dot{M}_{\text{Bondi}}(M)$  is the spherical Bondi rate for a single object of total mass  $M$ ,

$$\dot{M}_{\text{Bondi}} = 4\pi\lambda(\gamma)\rho_\infty c_\infty \left(\frac{GM}{c_\infty^2}\right)^2 = 4\pi\lambda(\gamma)\xi^{3/2} \quad (2)$$

with  $\lambda(\gamma)$  being the accretion coefficient (H. Bondi 1952),

$$\lambda = \frac{1}{4} \left(\frac{2}{5-3\gamma}\right)^{(5-3\gamma)/(2\gamma-2)}, \quad (3)$$

and  $\dot{M}_{\text{binary}}$  is the sum of the accretion rate onto both point masses in the binary problem.

Two scales govern the problem: the *geometric* compactness at which the accretion flows interact, and the *thermodynamic* threshold at which that interaction becomes destabilizing.

### 2.1. Geometric Scale

When  $\xi \ll 1$ , each component accretes independently. Since  $\dot{M}_{\text{Bondi}} \propto M^2$ , the combined efficiency is

$$\eta(\xi \ll 1) = \frac{1+q^2}{(1+q)^2}, \quad (4)$$

giving  $\eta = 1/2$  for equal masses. The sonic radius of component  $i$  accreting in isolation is

$$R_s^{(i)} = \frac{5-3\gamma}{4} \xi m_i = R_s m_i. \quad (5)$$

where  $R_s = (5-3\gamma)\xi/4$  is the dimensionless sonic radius for the total mass  $M$ . Setting  $R_s^{(1)} + R_s^{(2)} = 1$  gives the compactness at which the individual sonic surfaces make geometric contact:

$$\xi_m(\gamma) = \frac{4}{5-3\gamma}. \quad (6)$$

This is independent of  $q$ , and diverges as  $\gamma \rightarrow 5/3$ . The compactness  $\xi_m$  marks where the individual accretion flows first interact; whether that interaction leads to cooperative accretion or to instability depends on the thermodynamic response of the gas.

### 2.2. Sonic Surface Morphology

Before the sonic surfaces merge, the binary potential imprints a characteristic geometry on the transonic flow. At  $r \gg 1$ , the time-averaged potential of an equal-mass binary ( $q = 1$ ) is

$$\Phi(r, \theta) = -\frac{1}{r} \left[ 1 + \frac{1}{8} \left(\frac{1}{r}\right)^2 P_2(\cos \theta) + \mathcal{O}\left(\frac{1}{r}\right)^3 \right], \quad (7)$$

where  $\theta$  is the polar angle measured from the orbital axis,  $P_2$  is the Legendre polynomial. The quadrupolar perturbation deforms the spherical sonic surface into  $\mathcal{R} = R_s + \delta\mathcal{R}$ , with fractional amplitude

$$\frac{\delta\mathcal{R}}{R_s} \sim \frac{1}{8} \left(\frac{1}{R_s}\right)^2 = \frac{2}{(5-3\gamma)^2 \xi^2}, \quad (8)$$

which grows as  $\xi$  decreases or  $\gamma \rightarrow 5/3$ . The perturbation rotates at  $\Omega = 1$ , producing an  $m = 2$  spiral pattern in the corotating frame. T. Foglizzo & M. Ruffert (1997) proved that any detached sonic surface must intersect

$R_s$  at least once; in the binary case this constrains the deformation to two trailing spiral arms connecting the individual Bondi spheres to the shared transonic flow.

For  $\gamma = 5/3$ ,  $R_s = 0$  identically: no detached sonic surface exists at any  $\xi$ . The flow is always of Type SF or FSF in the T. Foglizzo & M. Ruffert (1997) classification – the sonic surface is attached to the accretors and directly exposed to the orbital dynamics. Whether these spirals remain stationary or become unstable depends on the entropy they carry.

### 2.3. Thermodynamic Scale: Shock-Driven Instability

The binary orbit introduces irreversible entropy generation absent in single-body Bondi accretion. Whether this entropy destabilizes the transonic flow depends on three factors: the rate of generation, the non-axisymmetry of the source, and whether the sonic sphere can confine the heated gas.

#### 2.3.1. Propeller Mach number

The gravitational potential of the binary is a quadrupolar pattern rotating at  $\Omega = 1$  in the inertial frame. In the corotating frame, this potential is time-independent. Gas falling from infinity with zero angular momentum has  $v_\phi = 0$  in the inertial frame; transforming to the corotating frame gives an azimuthal velocity  $v'_\phi = -\Omega r \sin\theta$  at position  $(r, \theta)$ , where  $\theta$  is the polar angle measured from the orbital axis. The gas therefore streams through the static corotating potential at azimuthal speed  $\Omega r \sin\theta$ .

The sound speed at  $r = 1$  follows from adiabatic compression during infall. In the supersonic interior ( $r < R_s$ ), mass conservation in the freefall regime gives  $\rho \propto r^{-3/2}$ , so that  $c^2 \propto \rho^{\gamma-1} \propto r^{-3(\gamma-1)/2}$ . Evaluating at  $r = 1$  and normalizing to  $c_\infty$  at the Bondi radius gives  $c(1) = c_\infty \xi^{3(\gamma-1)/4}$ . (For  $\xi > \xi_m$  the binary sits inside the sonic surface and the freefall scaling applies; for  $\gamma = 5/3$ , the flow is everywhere marginally transonic and  $\rho \propto r^{-3/2}$  is exact.) The propeller Mach number – the ratio of the corotating azimuthal speed to the local sound speed – is therefore

$$\mathcal{M}_p(\theta) \equiv \frac{|v'_\phi|}{c(1)} = \xi^{(5-3\gamma)/4} \sin\theta, \quad (9)$$

which we evaluate at its maximum,  $\theta = \pi/2$  (the orbital plane):  $\mathcal{M}_p \equiv \xi^{(5-3\gamma)/4}$ . For  $\gamma < 5/3$  and  $\xi > 1$ ,  $\mathcal{M}_p > 1$ : the gas sweeps through the quadrupolar pattern supersonically. Shocks form only where  $\mathcal{M}_p \sin\theta > 1$ , i.e. outside a polar cone of half-angle  $\theta_c = \arcsin(\mathcal{M}_p^{-1})$ . For deeply embedded binaries ( $\mathcal{M}_p \gg 1$ ),  $\theta_c \rightarrow 0$  and nearly the full solid angle is shocked; at marginal compactness ( $\mathcal{M}_p \sim 2$ ),  $\theta_c \approx 30^\circ$  and gas accreting through the po-

lar funnels arrives unshocked. The entropy generation is therefore concentrated in the equatorial belt.

The non-axisymmetric component of the potential at  $r = 1$  is dominated by the quadrupole (Eq. 7), with amplitude  $\delta\Phi \sim q(1+q)^{-2}$ , yielding velocity perturbations  $\delta v \sim q(1+q)^{-2}$ . For equal masses,  $\delta v \approx 1/4$  – a finite-amplitude perturbation. Compressive phases steepen into shocks on the nonlinear acoustic timescale  $\tau_{\text{steep}} \sim c/[(\gamma+1)\omega\delta v]$  (§ 101 in L. D. Landau & E. M. Lifshitz 1959), with  $\omega = 2\Omega$  (the gas encounters two compression maxima per azimuthal circuit through the  $m = 2$  pattern). This gives

$$\Omega\tau_{\text{steep}} \sim \frac{(1+q)^2}{2q(\gamma+1)\mathcal{M}_p}, \quad (10)$$

the shock formation time in units of  $\Omega^{-1}$ . For  $q = 1$  and  $\mathcal{M}_p \gtrsim 1$ ,  $\Omega\tau_{\text{steep}} \lesssim 1$ : standing shocks form within a single orbital period in the corotating frame. For  $\mathcal{M}_p < 1$  the streaming is subsonic and the gas adjusts quasistatically through smooth pressure gradients; the flow remains isentropic. In the unperturbed Bondi profile,  $\mathcal{M}_p = 1$  identically for  $\gamma = 5/3$ : nonlinear steepening of the background flow is arrested at the marginally sonic threshold. The binary's finite-amplitude perturbation creates local regions where  $\mathcal{M}_p$  exceeds unity, but no global standing shock pattern forms in the co-rotating frame.

#### 2.3.2. Entropy generation

The dimensionless entropy jump across a shock (Eq. 1.85 in Y. B. Zel'dovich & Y. P. Raizer 1966):

$$\Delta s = \ln \left[ \frac{2\gamma\mathcal{M}_1^2 - (\gamma-1)}{\gamma+1} \right] - \gamma \ln \left[ \frac{(\gamma+1)\mathcal{M}_1^2}{(\gamma-1)\mathcal{M}_1^2 + 2} \right] \quad (11)$$

vanishes identically at  $\gamma = 1$  for all Mach numbers  $\mathcal{M}_1$  where subscript represents the upstream value. Expanding about this exact zero yields

$$\Delta s = (\gamma-1)g(\mathcal{M}_1) + \mathcal{O}((\gamma-1)^2), \quad (12)$$

where  $g(\mathcal{M}) \equiv (\mathcal{M}^4 - 1)/(2\mathcal{M}^2) - \ln\mathcal{M}^2$  is positive-definite for  $\mathcal{M} > 1$ . This is the leading term in an expansion about the isothermal zero, valid for shocks of arbitrary strength.

The upstream Mach number  $\mathcal{M}_1$  entering the Rankine–Hugoniot relation is the component of velocity *normal* to the shock front, measured in the shock frame. In the corotating frame, the gas streams through the static quadrupolar potential at azimuthal speed  $\mathcal{M}_p c(1)$ . The standing shocks that form from the steepened perturbation are generically oblique: gas hits the shock at angle  $\beta$  to the shock normal, so  $\mathcal{M}_1 =$

$\mathcal{M}_p \sin \beta \leq \mathcal{M}_p$ . The identification  $\mathcal{M}_1 \sim \mathcal{M}_p$  is therefore an upper bound on the shock strength; the true entropy generation per shock passage is reduced by an order-unity geometric factor that depends on the shock morphology. The essential scaling  $\Delta s \propto (\gamma - 1)$ , however, is exact: it follows from the equation of state and is independent of the shock geometry.

A uniform entropy offset merely shifts the Bondi solution to a new baseline; it does not destabilize the flow. What breaks the sonic point is an entropy *gradient* across streamlines. The binary potential is quadrupolar: streamlines at different azimuths encounter shocks of different strength and obliquity. The resulting entropy variation scales as

$$\delta s \sim (\gamma - 1) f(\mathcal{M}_p) \frac{q}{(1 + q)^2}, \quad (13)$$

where  $f(\mathcal{M}_p)$  is a positive-definite function that vanishes at  $\mathcal{M}_p = 1$  and grows for  $\mathcal{M}_p > 1$ ; its precise form depends on the shock geometry, but its existence requires only that different streamlines experience different compressions. For  $\gamma = 1$  the variation vanishes (no fuel); for  $\mathcal{M}_p = 1$  it vanishes (no shock); for  $q = 0$  it vanishes (no asymmetry). This entropy gradient violates the Schwarzschild stability criterion ( $ds/dr < 0$ ), seeding convective instability.

### 2.3.3. Annihilating the Saddle Point

Entropy generated at  $r \sim 1$  can only accumulate if the sonic surface encloses the binary. For  $\xi \geq \xi_m$ , the binary sits inside the sonic surface: acoustic signals cannot propagate outward through the supersonic infall, and the shocked gas is confined. Each orbit adds entropy to the trapped region. For  $\xi < \xi_m$ , the binary is in the subsonic exterior and acoustic perturbations disperse freely. Whether the accumulated entropy disrupts the transonic structure – and on what timescale – is determined by the energy budget.

The sonic surface is the separatrix of the Bondi saddle point. In the  $(r, v)$  phase plane, the critical point at  $R_s$  is an X-point: the transonic accretion branch and the transonic wind branch cross there, and every other trajectory is either purely subsonic or purely supersonic. The transonic accretion solution is the unique trajectory threading the saddle, selected by the eigenvalue at the critical surface. The global accretion rate is determined there, and only there.

Each binary orbit deposits an entropy increment  $\delta s \sim (\gamma - 1) f(\mathcal{M}_p) q / (1 + q)^2$  into the shocked gas at  $r \sim a$  (Eq. 13), generating a fractional pressure perturbation  $\delta P / P = \delta s$  at fixed density. The X-point at  $R_s$  is indifferent to conditions downstream of it: as long as the saddle persists, the transonic topology is intact and the

global accretion rate is still selected by the critical surface. The convective plumes born at  $r \sim a$  must propagate outward through the entire supersonic shell and deliver enough entropy to  $R_s$  to eliminate the X-point. The disruption condition is annihilation of the saddle itself.

Given the container condition  $\xi > \xi_m$  (Section 2.1), the sonic surface encloses the binary and the supersonic shell between  $r = 1$  and  $r = R_s$  is well defined. The mechanical energy cost of transporting the perturbation from source to separatrix, integrated over this shell, is

$$E_{\text{disrupt}} \sim \dot{M}_{\text{Bondi}} \left( \sqrt{\frac{\xi}{\xi_m}} - 1 \right). \quad (14)$$

This is a first-order estimate valid for  $\xi > \xi_m$ . At  $\xi = \xi_m$ , the source and the separatrix coincide and  $E_{\text{disrupt}} = 0$ : entropy is deposited directly at the X-point and no transport is required. For  $\xi \gg \xi_m$ ,  $E_{\text{disrupt}} \sim \dot{M}_{\text{Bondi}} \sqrt{\xi/\xi_m}$  grows with embedding because the shell between source and saddle grows. The quadrupolar perturbation at  $r = 1$  is undiminished – its amplitude is fixed by  $q/(1 + q)^2$  and independent of  $\xi$  – but the binary looks increasingly like a monopole as seen from  $R_s$ , since  $a/R_s \propto 1/\xi \rightarrow 0$ . The  $\sqrt{\xi/\xi_m}$  factor measures this transport cost.

The binary deposits energy via gravitational stirring at a rate  $\dot{E}_{\text{stir}} = \zeta \dot{M}_{\text{Bondi}}$ , where  $\zeta$  absorbs the entropy generation efficiency per shock, the retention fraction against advective losses into the sinks, and the acoustic coupling efficiency between  $r \sim a$  and  $R_s$ . All three factors satisfy  $\zeta \propto (\gamma - 1)$ : the exact Rankine–Hugoniot relation (Eq. 11) requires isothermal shocks to generate zero entropy, making the stirring thermodynamically inert regardless of Mach number. Over one orbital period  $\Delta E_{\text{orb}} = 2\pi\zeta \dot{M}_{\text{Bondi}}$ , and the number of orbits to annihilate the saddle is

$$N = \frac{E_{\text{disrupt}}}{\Delta E_{\text{orb}}} \sim \frac{1}{\zeta} \left( \sqrt{\frac{\xi}{\xi_m}} - 1 \right) \propto \frac{1}{\gamma - 1} \left( \sqrt{\frac{\xi}{\xi_m}} - 1 \right). \quad (15)$$

The magnitude of  $\zeta$  is not predicted from first principles. The observed onset of turbulence within  $\mathcal{O}(1)$ – $\mathcal{O}(10)$  orbits at  $\xi = \xi_m$  for  $\gamma = 4/3$  constrains  $\zeta \sim 0.1$ – $1$ : at threshold  $\sqrt{\xi/\xi_m} - 1 = 0$  and  $N$  is dominated entirely by  $\zeta$ , consistent with the rapid onset found numerically.

### 2.3.4. Limiting cases

As  $\gamma \rightarrow 1$ ,  $N \rightarrow \infty$  through  $\zeta \rightarrow 0$ : isothermal shocks deposit zero entropy by Eq. (11), the plumes carry no buoyancy, and the saddle point is never reached regardless of how long the binary orbits. The gas has infinite

specific heat; shock heating generates no usable entropy and the stirring is thermodynamically inert.

As  $\gamma \rightarrow 5/3$ ,  $\xi_m \rightarrow \infty$  (Section 2.1) and Eq. (15) never applies. In the freefall regime, both the infall velocity and the sound speed scale as  $r^{-1/2}$ ; their ratio is frozen and the flow is everywhere marginally transonic. No X-point exists at any finite radius, so there is no separatrix to protect the flow. The propeller shocks vanish ( $\mathcal{M}_p = 1$  generates no entropy jump), but the flow is nonetheless unstable: the binary potential creates finite-amplitude perturbations to the density and velocity fields, and in a  $\gamma = 5/3$  gas – where the adiabatic Bondi profile is neutrally stratified – any such perturbation produces entropy inversions that violate the Schwarzschild criterion ( $ds/dr < 0$ ), seeding convective instability. Turbulence at  $\gamma = 5/3$  is therefore thermodynamic in origin rather than shock-driven: it arises from entropy *rearrangement* by the binary potential in a flow with zero convective stability margin. The resulting turbulence is nonetheless shock-dominated in its saturated state: the convective velocities are transonic by construction ( $v/c \lesssim 1$  at all radii for  $\gamma = 5/3$ ), so the turbulent eddies themselves steepen into shocks (Section 4.3).

As  $\xi \rightarrow \infty$  ( $a \rightarrow 0$  at fixed  $M$  and  $c_\infty$ ),  $N \rightarrow \infty$  through the growing transport barrier  $\sqrt{\xi/\xi_m}$ : the shell between source and separatrix grows without bound, recovering the known stability of single Bondi accretion (H. Bondi 1952). The entropy generated per orbit involves a competition between fuel ( $\gamma - 1$ , increasing toward 5/3) and propeller strength ( $\mathcal{M}_p$ , decreasing toward 5/3), which peaks near  $\gamma \sim 1.2$ –1.4: the relativistic equation of state  $\gamma = 4/3$  sits in the most potent range.

We define breakout as the annihilation of the Bondi saddle point: the moment when cumulative entropy injection eliminates the X-point in the  $(r, v)$  phase plane and the transonic accretion solution ceases to exist as a smooth trajectory. Breakout of the convective region through the large-scale sonic surface requires three ingredients: (i) a *propeller* ( $\xi > 1$ ,  $\gamma < 5/3$ ): the pattern moves supersonically and generates shocks; (ii) *fuel* ( $\gamma > 1$ ): the post-shock gas retains entropy and develops convectively unstable gradients; and (iii) a *container* ( $\xi > \xi_m$ ): a finite sonic surface confines the heated bubble. When all three are satisfied, breakout is inevitable in the absence of radiative cooling and occurs on the timescale given by Eq. (15). Cooling introduces a fourth condition: the cooling time at  $r \sim 1$  must exceed  $NT$ , where  $T$  is the orbital period. When  $t_{\text{cool}} \ll NT$ , post-shock entropy is radiated before it accumulates, and the gas behaves as effectively isothermal regardless of its

microscopic  $\gamma$ . The single comparison  $t_{\text{cool}}$  versus  $NT$  therefore governs whether a given astrophysical system falls in the cooperative or turbulent regime.

### 3. NUMERICAL METHODOLOGY

The problem requires resolving the interaction between a global sonic surface at  $r \sim \xi$  and the vacuum-like accretion funnels at  $r \sim 1$ , spanning Mach numbers from  $\mathcal{M} \sim 0$  at stagnation points to  $\mathcal{M} \gg 1$  in the free-fall region. We carry out this numerical experiment using the open-source Godunov-type gas dynamics code SIMBI (M. DuPont 2023).

#### 3.1. Governing Equations

We solve the Newtonian continuity and Euler equations,

$$\frac{\partial \rho}{\partial t} + \nabla \cdot (\rho \mathbf{v}) = S_\rho, \quad (16)$$

$$\frac{\partial(\rho \mathbf{v})}{\partial t} + \nabla \cdot (\rho \mathbf{v} \otimes \mathbf{v} + P\mathbb{I}) = -\rho \nabla \Phi + \mathbf{S}_{\rho \mathbf{v}}, \quad (17)$$

$$\frac{\partial \mathcal{E}}{\partial t} + \nabla \cdot [(\mathcal{E} + P)\mathbf{v}] = -\rho \mathbf{v} \cdot \nabla \Phi + S_\mathcal{E}, \quad (18)$$

where  $\rho$  is the fluid density,  $\mathbf{v}$  the velocity field,  $P$  the pressure, and  $\mathcal{E} = \frac{1}{2}\rho v^2 + \epsilon_{\text{int}}$  the total energy density with  $\epsilon_{\text{int}}$  being the internal energy density. The source terms  $S_\rho, \mathbf{S}_{\rho \mathbf{v}}, S_\mathcal{E}$  represent explicit removal of mass, momentum, and energy by the point masses (M. R. Krumholz et al. 2004). The gravitational potential is

$$\Phi(\mathbf{r}, t) = - \sum_{i=1}^2 \frac{M_i}{\sqrt{|\mathbf{r} - \mathbf{r}_i(t)|^2 + \ell_i^2}}, \quad (19)$$

where  $\mathbf{r}_i(t)$  is the position of mass  $i$  and the softening length  $\ell_i$  is fixed at 1% of the individual Bondi radius. We close the system with a gamma-law equation of state,  $P = (\gamma - 1)\epsilon_{\text{int}}$ , and investigate two thermodynamic limits: isothermal ( $\gamma = 1$ ) to isolate the pure gas-dynamic response to the binary potential, and adiabatic ( $\gamma > 1$ ) to explore the role of shock heating. For the isothermal case, uniform initial conditions ( $\rho_\infty, c_\infty$ ) are numerically stable; the adiabatic runs required mild energy floors at start up ( $\epsilon_{\text{floor}} = 10^{-6}$  in code units, six orders of magnitude below the ambient thermal energy density) for  $\xi = 10$ .

We evolve Equations 16–18 with the HLLC Riemann solver (A. Harten et al. 1983; B. Einfeldt 1988) and piecewise linear reconstruction (Minmod,  $\theta_{\text{plm}} = 1$ ) across active zones and piecewise parabolic reconstruction across level boundaries to cancel out the order of spatial accuracy loss (M. J. Berger & P. Colella 1989). The HLLC solver is chosen for its positivity-preserving

property – essential in the evacuated regions between accretors – and because its numerical dissipation at contact discontinuities suppresses the persistent oscillations that contact-resolving schemes (e.g., HLLC, Roe) excite at the standing shocks characteristic of this problem.

### 3.2. The Telescoping Grid

To bridge the scale separation of  $\xi \sim 10$  without prohibitive cost, we implement a telescoping grid using fixed mesh refinement (FMR), a static variant of the adaptive mesh refinement framework of M. J. Berger & P. Colella (1989). The grid hierarchy is a sequence of nested Cartesian patches centered on the origin. The base grid covers  $\pm R_{\text{out}} = \max(4R_B, 4a)$ , ensuring the outer boundary is causally disconnected from the binary’s acoustic feedback for the duration of each simulation. Each successive level halves the semi-width and doubles the resolution, maintaining a constant zone count per patch. The finest level covers the orbital domain ( $r \leq 1.5$ ) at  $\Delta x_{\text{fine}} = 1/64$ , decreased to  $1/256$  for  $\xi = 0.1$  to place at least 5–10 zones inside the sonic surface or Bondi surface for the runs where there is no sonic surface.

### 3.3. Convergence

The accretion efficiency  $\eta = \dot{M}_{\text{binary}}/\dot{M}_{\text{Bondi}}$  is a ratio of two quantities computed with identical sink prescriptions: the same removal radius  $r_{\text{acc}}$ , the same softening length  $\ell$ , and the same energy floor. Any systematic bias introduced by the sink enters both numerator and denominator and cancels in the ratio. This self-calibration is the principal reason  $\eta$  is the appropriate accretion metric.

Two dimensionless ratios control the residual sensitivity to the sink. The first is  $r_{\text{acc}}/R_s$ : the sink must lie well inside the sonic surface so that the transonic structure that sets  $\dot{M}_{\text{Bondi}}$  is resolved. We find that the single-accretor rate converges to the analytic Bondi solution within  $\lesssim 3\%$  once  $r_{\text{acc}}/R_s \lesssim 0.1$ , consistent with the resolution requirements identified by M. Ruffert (1994) and M. R. Krumholz et al. (2004). The second is  $r_{\text{acc}}/a$ : the sink must be small compared to the binary separation so that the two accretion funnels are resolved as distinct objects. With  $r_{\text{acc}}/R_s$  held fixed at a value satisfying the first condition, we vary  $r_{\text{acc}}/a$  over a decade (0.10, 0.05, 0.01) and find that the time-averaged  $\eta$  in statistical steady state changes by less than 5%. The softening length  $\ell/a$  was tested independently at 0.10, 0.05, and 0.01 with no significant change in  $\eta$ . The insensitivity of  $\eta$  to both  $r_{\text{acc}}/a$  and  $\ell/a$  confirms that the accretion suppression is governed by the thermodynamic structure at  $r \sim a - R_s$  – the entropy bubble and the sonic surface – rather than by the details of mass removal near each component.

For  $\gamma = 5/3$ , the Bondi solution has no detached sonic point:  $R_s = 0$  identically, and the condition  $r_{\text{acc}}/R_s \ll 1$  is undefined. The absolute accretion rate retains a residual dependence on  $r_{\text{acc}}$ , as noted by M. Ruffert (1994). However, both  $\dot{M}_{\text{binary}}$  and  $\dot{M}_{\text{single}}$  are computed with the same  $r_{\text{acc}}$ , and the  $r_{\text{acc}}$ -dependence cancels in  $\eta$ . We verify this explicitly:  $\eta(\xi)$  at  $\gamma = 5/3$  is unchanged when  $r_{\text{acc}}/a$  is varied over the same decade. This is the stronger convergence statement – neither numerator nor denominator converges individually, but their ratio does – and it confirms that  $\eta$  measures a property of the binary’s thermodynamic interaction with the gas. At  $\xi = 0.1$ , the softening length  $\ell$  falls below the grid scale on the finest level; the insensitivity of  $\eta$  to  $\ell/a$  over a decade confirms that this does not affect the results.

### 3.4. Boundary Conditions

We employ a relaxation boundary condition in the outer 20% of the domain ( $R_{\text{buf}} > 0.8R_{\text{out}}$ ), applying a source term that drives the flow toward the analytic Bondi profile for a monopole of mass  $M$ :

$$\frac{\partial U}{\partial t} = \dots - \frac{1}{\tau_{\text{damp}}} \mathcal{S}(r) (U - U_{\text{Bondi}}), \quad (20)$$

where  $\mathcal{S}(r)$  is a cubic smoothstep with values in  $[0, 1]$ ,  $U$  the conserved state,  $U_{\text{Bondi}}$  the target Bondi state, and  $\tau_{\text{damp}}$  the lesser of the sound-crossing time across the buffer zone and half the orbital period. This ensures the asymptotic far-field mass flux,

$$\dot{M}_{\text{buf}}(r) \approx 4\pi\lambda(\gamma)\xi^{3/2} \left[ 1 - \frac{1}{4} \left( \frac{\xi}{r} \right)^2 \right], \quad (21)$$

is obeyed, with  $\lambda(\gamma)$  being the eigenvalue from the Bondi solution. This active boundary ensures that the mass supply is determined by the cloud thermodynamics rather than by artificial reflection or rarefaction waves. Relaxing the full conserved state (density, momentum, and energy) is essential. With standard outflow boundary conditions, the domain depletes faster than gas can be resupplied: the accretion rate falls below the theoretical Bondi value even for a single accretor, as the finite mass reservoir is exhausted before a steady state is reached. The relaxation boundary continuously replenishes the outer domain toward the analytic profile, ensuring an effectively infinite mass supply and allowing the flow to settle to its true steady state. We emphasize that this active boundary controls the *supply* of gas at  $r \sim R_{\text{out}}$ , not the accretion rate onto the point masses; the interior flow is free to find whatever steady state the local thermodynamics demands.

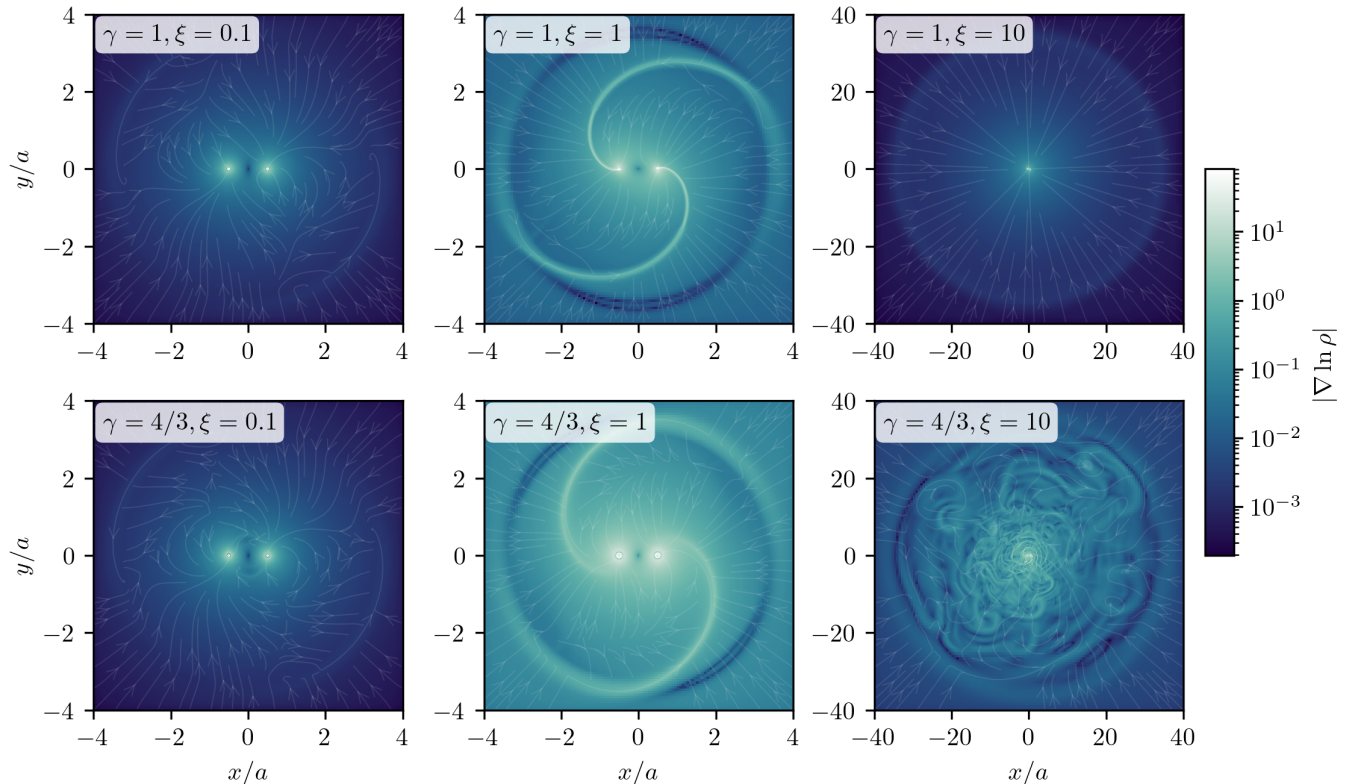


**Figure 1.** Density gradient schlieren  $|\nabla \ln \rho|$  with velocity streamlines overlaid, showing flow morphology across compactness  $\xi$  for isothermal ( $\gamma = 1$ , top) and relativistic ( $\gamma = 4/3$ , bottom) gas. Isothermal flows remain stationary and organized at all  $\xi$ : independent accretion at  $\xi = 0.1$ , coherent spiral structure at  $\xi = 1$ , and radial monopole-like inflow at  $\xi = 10$ . Polytropic flows exhibit similar organization at low  $\xi$  but become turbulent at high  $\xi$ :  $\xi = 10$  shows complete loss of coherent structure with chaotic, multi-scale density fluctuations. The transition from organized to turbulent occurs between  $\xi = 1$  and  $\xi = 10$  for  $\gamma = 4/3$ , consistent with the predicted threshold Eq. (6) where shock-generated entropy overwhelms the sonic buffer. All above plots are shown at  $t \geq 3t_B$  for each respective  $\xi$ .

#### 4. RESULTS

All simulations are evolved for at least  $3t_B$  after transients decay where  $t_B = R_B/c_\infty = \xi^{3/2}$  is the characteristic Bondi time. Statistics are computed over 5-orbit windows for  $t > t_B$ . We present the flow morphology, turbulence diagnostics, temporal variability, and accretion efficiency in turn.

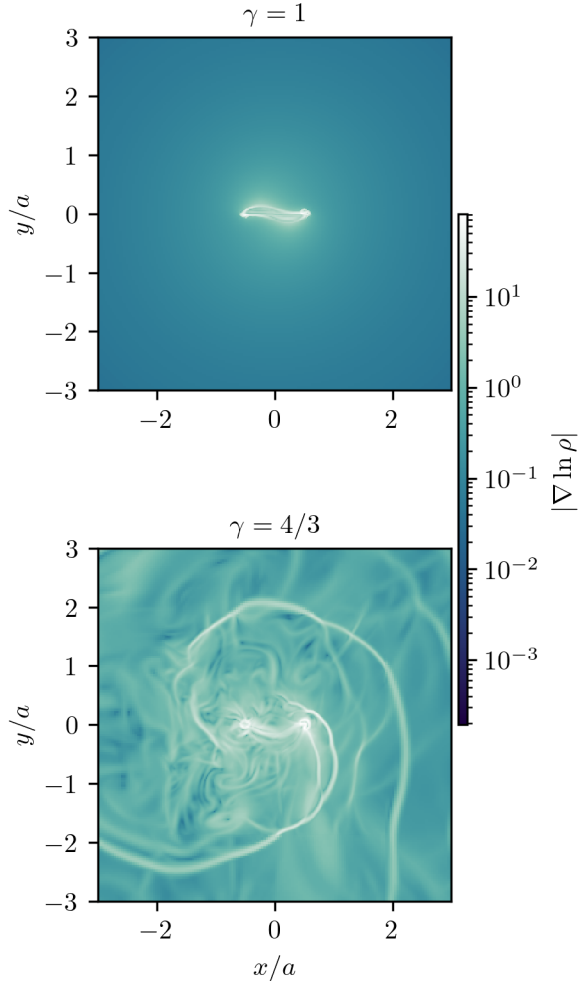
##### 4.1. Flow Morphology

Figure 1 shows density gradient schlieren  $|\nabla \ln \rho|$  with velocity streamlines for  $\gamma = 1$  (top) and  $\gamma = 4/3$  (bottom) across  $\xi = 0.1, 1$ , and  $10$ . The smooth transitions visible at large radii in each figure is the imprint of the relaxation buffer (Section 3.4). The flow is driven toward the analytic Bondi profile in the outer 20% of the domain, producing a featureless gradient there by construction. All physical structures discussed below lie well inside this buffer region.

For isothermal gas, the flow is stationary in the corotating frame at all  $\xi$ . At  $\xi = 0.1$  the components accrete independently, each with its own Bondi sphere. At  $\xi = 1$

the sonic surfaces interact, producing a coherent  $m = 2$  spiral shock pattern. At  $\xi = 10$  the spiral arms have merged into a high-density bridge connecting the two components, and the outer flow is indistinguishable from radial monopole infall. The bridge is the mechanism by which  $\eta \rightarrow 1$ : it channels mass directly to the individual accretion funnels through a shared high-density stream. Figure 2 shows the orbital-scale structure at  $\xi = 10$  in detail: the isothermal bridge is smooth and laminar, with no shocks outside the immediate vicinity of the accretors.

For  $\gamma = 4/3$ , the flow at  $\xi = 0.1$  and  $\xi = 1$  is organized and qualitatively similar to the isothermal case, with coherent spiral structure in the corotating frame. At  $\xi = 10$  the flow is fully turbulent: the spiral pattern has been destroyed, replaced by chaotic, multi-scale density fluctuations filling the domain to  $r \sim 30a$ . At the orbital scale (Figure 2), two shocks tracing the  $m = 2$  pattern at  $r \sim 2a$  marks the disrupted sonic surface; inside it, filaments, vortices, and secondary shocks fill the cavity. The transition between organized and tur-



**Figure 2.** Density gradient schlieren  $|\nabla \ln \rho|$  in the orbital plane at  $t = 3t_B$  for  $\xi = 10$ , zoomed to  $r \leq 3a$ . *Top:* for  $\gamma = 1$ , the flow is laminar; the only structure is the high-density bridge connecting the two accretors. *Bottom:* for  $\gamma = 4/3$ , shocks co-rotating with the binary at  $r \sim 2a$  marking the disrupted sonic surface. Inside it, the flow is fully turbulent – filaments, vortices, and secondary shocks fill the interior. This is the entropy instability in action: orbital stirring drives shocks that generate entropy, inflating the post-shock gas and destroying the transonic structure.

turbulent flow occurs between  $\xi = 1$  and  $\xi = 10$ , consistent with the predicted threshold  $\xi_m = 4$  at which the sonic surface first encloses the binary (Section 2.3).

Figure 3 shows the same diagnostic for  $\gamma = 5/3$ . The flow is disordered at all  $\xi$ , including  $\xi = 0.1$  where the orbital Mach number is subsonic. At  $\xi = 10$  the turbulence fills the domain out to  $\sim 30a$  with no coherent large-scale structure. The absence of a detached sonic surface means there is no causal membrane shielding the outer flow from the binary’s gravitational stirring: perturbations propagate outward without impediment.

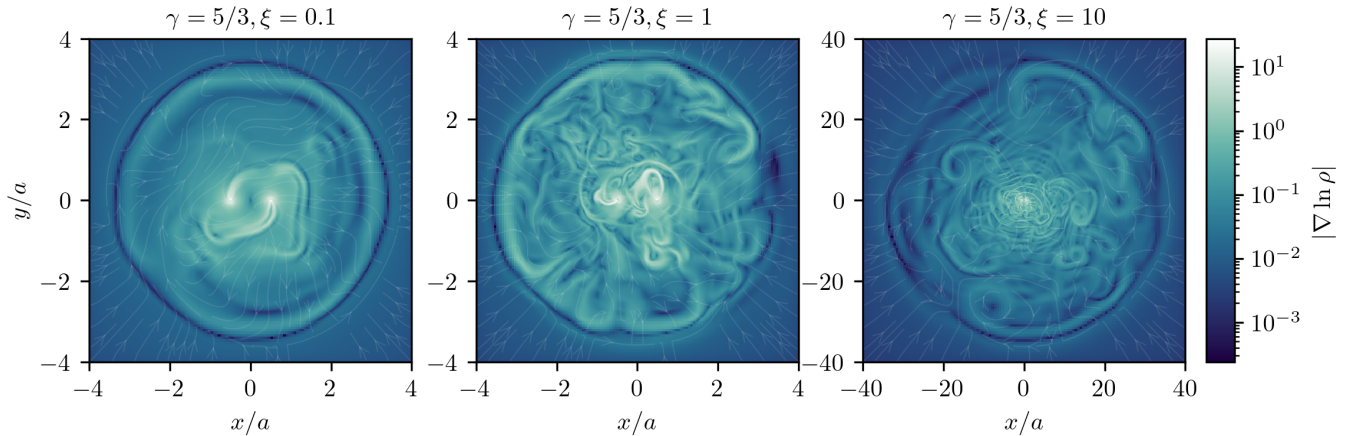
#### 4.2. Radial flow structure

Figure 4 shows time- and angle-averaged radial profiles of the density  $\langle \rho \rangle$ , squared sound speed  $\langle c^2 \rangle$ , absolute radial velocity  $\langle |v_r| \rangle$ , and turbulent velocity dispersion  $\langle \delta v \rangle$  at  $\xi = 10$  for each  $\gamma$ . Profiles are averaged over spherical shells centered on the binary center of mass for  $r > a$ , and over the quasi-steady-state interval  $t > 10$  orbits. The velocity dispersion is computed via Reynolds decomposition: for each cell, the time-mean velocity is subtracted before computing the root-mean-square (RMS) fluctuation, so  $\delta v$  measures genuine temporal variability rather than organized non-radial flow (e.g. the high-density bridge in the isothermal case). Gray dotted lines show the analytic Bondi solution for each  $\gamma$  (with the exception of the  $\propto r^{-1}$  line shown for  $\langle \rho \rangle$ ); light traces show the temporal variance of the angle-averaged profiles over the averaging interval of one orbit.

For  $\gamma = 1$ , all four profiles track the analytic Bondi solution reasonably well. The density follows  $\rho \propto r^{-3/2}$  in the supersonic interior, the sound speed is constant by construction, and the radial velocity follows the freefall scaling  $|v_r| \propto r^{-1/2}$ . The velocity dispersion is negligible ( $\delta v/|v_r| \lesssim 10^{-2}$ ), confirming that the flow is laminar and steady.

For  $\gamma = 4/3$ , the flow roughly tracks the expected Bondi profile even though the flow is turbulent. For  $\gamma = 5/3$ , the profiles deviate from the Bondi solution inside  $r \sim 5a$ . The density flattens to  $\rho \propto r^{-1}$ , shallower than the freefall scaling. The “temperature” profiles of the adiabatic flows, by contrast, are largely unaffected: the squared sound speed follows  $c^2 \propto r^{-3(\gamma-1)/2}$  – the canonical Bondi scaling – for both  $\gamma = 4/3$  and  $\gamma = 5/3$ . The entropy instability redistributes gas spatially, flattening the density profile for the stiffer gas ( $\gamma = 5/3$ ), but preserves the temperature stratification set by the gravitational potential.

The velocity structure reveals the mechanism of suppression. The radial infall velocity drops to one to two orders of magnitude below the freefall value for both adiabatic cases. The turbulent velocity dispersion, measured via Reynolds decomposition, reaches  $\delta v \sim 0.1$ – $1 c_\infty$  in the interior, exceeding the coherent radial infall by a factor of a few to  $\sim 10$  for  $\gamma = 4/3$  and  $\sim 10$ – $100$  for  $\gamma = 5/3$  in the interior ( $r \lesssim 10a$ ). The flow is not accreting in any organized sense: large-scale convective eddies circulate gas through the Bondi sphere, and accretion proceeds as a small net residual of nearly cancelling inflow and outflow. The temporal variance in  $|v_r|$  (light traces) is comparable to the mean itself for  $\gamma > 1$ , while the variance in  $\delta v$  is modest – the turbulence is statis-



**Figure 3.** Density gradient schlieren  $|\nabla \ln \rho|$  for  $\gamma = 5/3$  in the orbital plane at  $t \geq 3t_B$ . The flow is disordered at all  $\xi$ : no sonic surface exists to shield the outer flow. Turbulent structure extends to  $\sim 30a$  at  $\xi = 10$ .

tically steady even as the instantaneous radial velocity fluctuates wildly.

The  $\rho \propto r^{-1}$  inner scaling matches the density profiles found in a number of previous studies, including turbulent non-radiative accretion onto a point mass in hydrodynamics and MHD (M. Guo et al. 2023; H. Cho et al. 2023; M. Guo et al. 2025). That the same scaling emerges here – from purely hydrodynamic, binary-driven stirring rather than magnetic turbulence or externally imposed hydrodynamic turbulence – suggests the inner profile is set by the convective equilibrium of the envelope rather than by the mechanism that seeds the turbulence (e.g., S. M. Ressler et al. 2020). This universality reinforces the connection between the binary Bondi problem and the broader convection-dominated accretion flow / radiatively inefficient accretion flow literature: in both cases, the accretion rate at small radii is governed by the turbulent transport properties of the envelope.

#### 4.3. Turbulence Character

We characterize the irreversible entropy field via the angular power spectrum of  $\kappa \equiv P/\rho^\gamma$ . Since  $\kappa$  is an adiabatic invariant – constant along streamlines in the absence of shocks – all spatial structure in  $\kappa$  traces entropy generation rather than organized flow. At each radius  $r$ , we interpolate  $\kappa$  onto a regular equirectangular grid in  $(\theta, \phi)$ , subtract the shell mean, and compute the angular power spectrum via 2D fast Fourier transform (FFT) with  $\sin \theta$  quadrature weighting:

$$C_\ell^{(\kappa)}(r) = \frac{1}{2\ell + 1} \sum_{m=-\ell}^{\ell} |\hat{\kappa}_{\ell m}(r)|^2, \quad (22)$$

where  $\hat{\kappa}_{\ell m}$  are the 2D Fourier coefficients of the weighted fluctuation field  $\delta\kappa \sin \theta$ , and the physical wavenum-

ber is  $k = \ell/r$  in units of  $\text{rad}/a$ . The 2D FFT on an equirectangular grid approximates a true spherical harmonic transform; the approximation is adequate for power-law slope estimation but not for absolute amplitudes at low  $\ell$ . Spectra are averaged over seven logarithmically spaced shells spanning  $r/a \in [1, 10]$ , interior to the Bondi radius  $R_B = 10a$ .

For  $\gamma = 1$ , the spectrum sits at machine precision ( $C_\ell \sim 10^{-38}$ ) at all scales, confirming that the isothermal flow generates no entropy despite the presence of shocks and spiral structure. This null test establishes that the signal in the adiabatic cases reflects genuine entropy fluctuations rather than numerical or geometric artifacts.

For  $\gamma = 4/3$  and  $5/3$ , the spectra are elevated by orders of magnitude. The  $\gamma = 5/3$  spectrum carries more power than  $\gamma = 4/3$  at all scales, consistent with more vigorous large-scale entropy rearrangement driven by convection in the neutrally stratified flow. Both adiabatic spectra follow  $k^{-3.5 \pm 0.1}$  over the resolved range  $k \sim 0.5\text{--}6 \text{ rad}/a$ . This slope is steeper than standard cascade predictions (e.g.,  $k^{-5/3}$  Kolmogorov or  $k^{-2}$  Burgers), consistent with a spectrum dominated by isolated coherent structures rather than a volume-filling cascade. It is consistent with the coherent structures visible in the density gradient images (Figures 1–3).

The two adiabatic cases have distinct physical origins despite their similar spectral slopes. For  $\gamma = 4/3$ , the causal chain runs from the supersonic propeller to standing orbital shocks, to entropy accumulation, to breakout: shocks *cause* the instability. For  $\gamma = 5/3$ , the propeller is marginally sonic ( $\mathcal{M}_p = 1$ ) and generates no standing shocks in the corotating frame; the instability is convective, driven by entropy rearrangement in a neutrally stratified flow. The resulting convective velocities are of order  $v_{\text{orb}}$  in a gas where  $v/c \sim 1$  at all radii, so the tur-

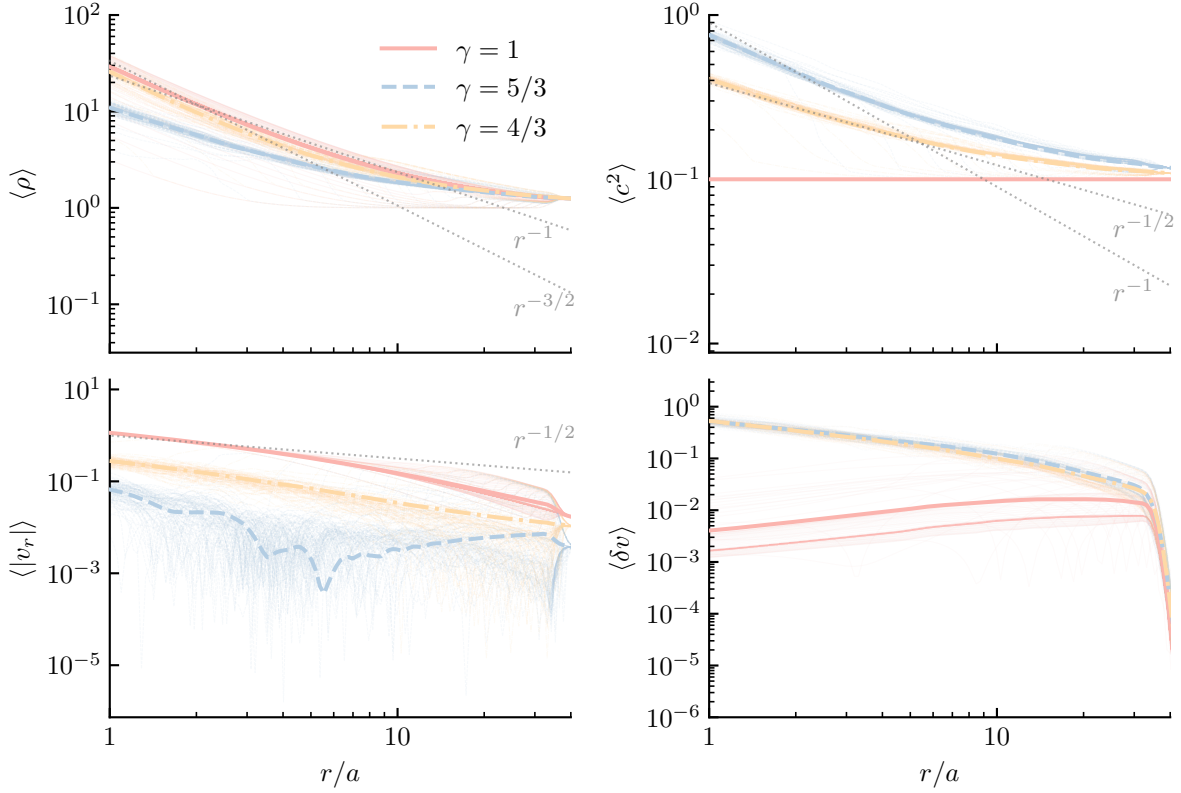


**Figure 4.** Time- and angle-averaged radial profiles at  $\xi = 10$ : density (top left), squared sound speed (top right), absolute radial velocity (bottom left), and turbulent velocity dispersion via Reynolds decomposition (bottom right). Gray dotted lines show the analytic Bondi profiles; reference power laws are labeled. Lighter traces show the temporal variance of the angle-averaged profiles. For  $\gamma = 1$  (solid, pink), all profiles track the Bondi solution and  $\delta v$  is negligible: the flow is laminar. For  $\gamma = 4/3$  (dash-dotted yellow), the density profile obeys the Bondi character reasonably well, but the  $\gamma = 5/3$  flattens towards  $\rho \propto r^{-1}$  inside  $r \sim 5a$  while the temperature profiles  $c^2 \propto r^{-3(\gamma-1)/2}$  for both are preserved. The radial velocity is suppressed by factors of a few below freefall; the turbulent dispersion exceeds it by a factor of a few to  $\sim 10$ , confirming that the interior is a turbulence-dominated reservoir with accretion as a residual.

bulent motions produce shocks in the saturated state. The similar  $k^{-7/2}$  slopes reflect similar shock front morphology in the saturated state, not a common driving mechanism.

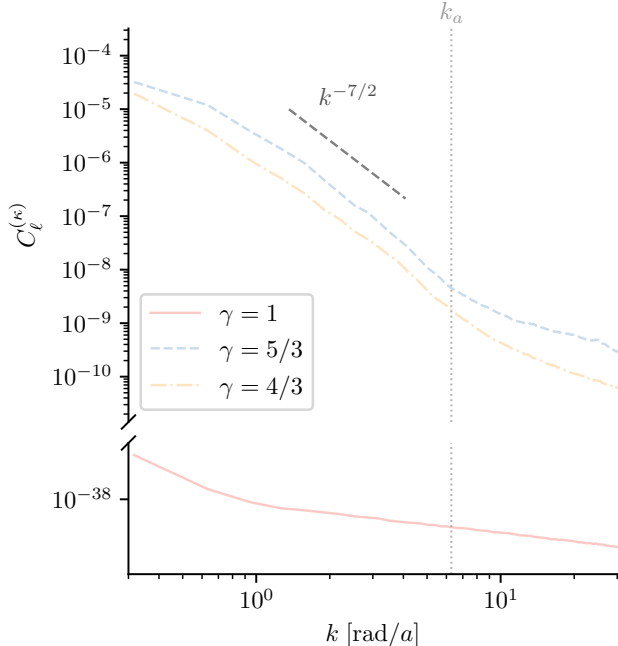
#### 4.4. Temporal Variability

Figure 6 shows Lomb-Scargle periodograms of the total accretion rate  $\dot{M}_{\text{tot}}(t)$  (dark) and the individual component rates  $\dot{M}_{1,2}(t)$  (light) at  $\xi = 10$  for each  $\gamma$ . Since in practice the emission from each component can dominate a distinct spatial region, the individual periodograms can also be an observationally relevant quantity.

For  $\gamma = 5/3$  (top), both the total and individual periodograms are pure broadband noise with no coherent feature at any orbital harmonic. The turbulence has completely erased the orbital signal. For  $\gamma = 4/3$  (middle), a residual peak at  $2\Omega$  rises  $\sim 5\text{--}10\times$  above the turbulent continuum in both the total and individual rates. The  $2\Omega$  dominance reflects the equal-mass sym-

metry: the  $q = 1$  potential repeats every half orbit. The orbital signature survives but is partially buried in turbulent noise. For  $\gamma = 1$  (bottom), both the individual component rates and the total show coherent peaks at  $4\Omega$  and  $8\Omega$ , with no significant power at  $2\Omega$ . The accretion rate responds nonlinearly to the  $2\Omega$  quadrupolar forcing, transferring power to the first overtone and its harmonic. An observer would detect periodicity at  $4\Omega$  and infer half the true orbital period.

The broadband floor in the  $\gamma = 1$  panel is elevated relative to the adiabatic cases and is a numerical artifact: the isothermal flow concentrates mass into a narrow high-density bridge between the two accretors, and the finite accretion kernel clips this filament differently at each timestep, producing rapid oscillations in the instantaneous  $\dot{M}$  at frequencies well above the orbital harmonics. For  $\gamma = 4/3$  and  $\gamma = 5/3$ , turbulence broadens density gradients over many cells and the kernel integral is smooth, suppressing this artifact despite the stronger physical variability in those cases. The relevant diag-



**Figure 5.** Angular power spectrum of the entropy proxy  $\kappa = P/\rho^\gamma$  at  $\xi = 10$ . For each of seven logarithmically spaced shells in  $r/a \in [1, 10]$ , the fluctuation field  $\delta\kappa = \kappa - \langle\kappa\rangle_{\text{shell}}$  is interpolated onto an equirectangular  $(\theta, \phi)$  grid and decomposed via 2D FFT with  $\sin\theta$  weighting; the resulting  $C_\ell$  are averaged across shells and mapped to spatial wavenumber  $k = \ell/r$ . The isothermal case ( $\gamma = 1$ ) returns  $C_\ell \sim 10^{-38}$  at all scales, confirming that the adiabatic spectra reflect genuine entropy production rather than numerical or geometric artifacts. Both  $\gamma = 5/3$  and  $\gamma = 4/3$  follow  $k^{-7/2}$  over the resolved range  $k \lesssim k_a$ , steeper than Kolmogorov ( $k^{-5/3}$ ) or Burgers ( $k^{-2}$ ) scaling, consistent with a spectrum set by isolated shock fronts and convective boundaries rather than a volume-filling cascade. The  $\gamma = 5/3$  spectrum carries more power at all scales, reflecting larger per-shock entropy jumps in the stiffer equation of state. The upturn above  $k_a$  is a pixel window artifact of the equirectangular interpolation and should not be interpreted as physical.

nistic is therefore peak height above the noise floor and not absolute power. By this measure the coherent peaks at  $4\Omega$  and  $8\Omega$  in the  $\gamma = 1$  case rise 1–1.5 decades above the artifact floor and are robust.

The progression from broadband noise ( $\gamma = 5/3$ ) through marginal detection ( $\gamma = 4/3$ ) to coherent periodicity ( $\gamma = 1$ ) has direct implications for binary AGN searches: the thermodynamic regime of the ambient gas determines not only the accretion efficiency but also the detectability of the orbital signal.

#### 4.5. Accretion Efficiency

Figure 7 shows the accretion efficiency  $\eta \equiv \dot{M}_{\text{binary}}/\dot{M}_{\text{Bondi}}$  as a function of  $\xi$  for each  $\gamma$ . Error bars

span the 10th–90th percentile of  $\eta(t)$ . For  $\gamma = 1$ ,  $\eta$  rises monotonically from  $\approx 0.5$  at  $\xi = 0.1$  to  $\approx 1$  at  $\xi = 10$ . At low  $\xi$  the components accrete independently, recovering the predicted  $\eta = 1/2$  for equal masses (Eq. 4). At high  $\xi$  the bridge channels mass cooperatively and  $\eta \rightarrow 1$ .

For  $\gamma = 4/3$ ,  $\eta$  tracks the independent rate at low  $\xi$ , rising from  $\approx 0.42$  at  $\xi = 0.1$  to  $\approx 0.51$  at  $\xi = 1$ . Beyond the container threshold  $\xi_m = 4$ ,  $\eta$  drops sharply to  $\approx 0.32$  at  $\xi = 10$ . The turbulence does not merely prevent cooperation – it actively suppresses accretion below the independent rate. The overpressured, entropy-laden gas resists infall more effectively than the undisturbed Bondi profile.

Both  $\gamma = 1$  and  $\gamma = 4/3$  flows develop spiral shocks at  $\xi = 1$ , yet the isothermal efficiency already exceeds  $1/2$  while the polytropic efficiency does not. The distinction lies in what the shock does to the gas. An isothermal shock dissipates kinetic energy that is radiated away instantaneously: the gas decelerates without pressurizing, making it easier to capture. The spiral arms actively assist accretion by removing the kinetic energy that would otherwise carry gas past the accretor. An adiabatic shock converts kinetic energy into thermal energy: the gas decelerates but heats up, and the resulting pressure cushion resists further infall. The funneling effect of the spiral arms and the post-shock pressurization nearly cancel, leaving  $\eta \approx 1/2$ .

For  $\gamma = 5/3$ ,  $\eta$  is suppressed at all  $\xi$ , ranging from  $\approx 0.27$  at  $\xi = 0.1$  to  $\approx 0.10$ – $0.12$  at  $\xi \geq 1$ . The error bars are small, reflecting saturated turbulence with steady suppression rather than organized flow. The absence of a threshold in  $\xi$  is consistent with the geometric instability of the attached sonic surface.

## 5. DISCUSSION

An embedded binary in adiabatic gas is self-limiting: the orbit that gravitationally drives accretion simultaneously generates the entropy that disrupts it. We discuss the implications for accretion physics, binary detection, and specific astrophysical systems.

### 5.1. A Third Route to Convection-Dominated Accretion

Two routes to convectively unstable accretion are known: dissipation of rotational energy in rotating advection-dominated flows (R. Narayan & I. Yi 1994, 1995), potentially producing the CDAF regime (J. M. Stone et al. 1999; I. V. Igumenshchev & M. A. Abramowicz 2000; R. Narayan et al. 2000; E. Quataert & A. Gruzinov 2000), and the dissipation of magnetic energy in magnetized accretion from a uniform medium (I. V. Igumenshchev & R. Narayan 2002).

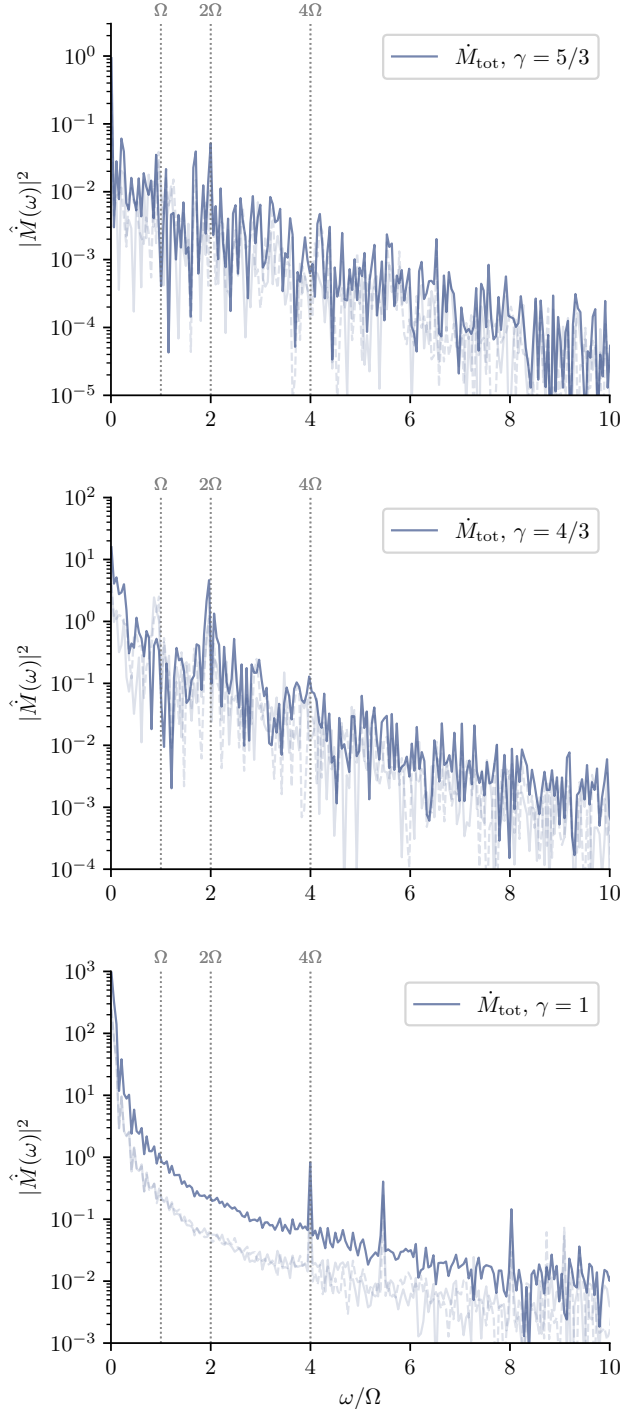


**Figure 6.** Lomb–Scargle periodograms of  $\dot{M}_{\text{tot}}(t)$  (dark) and individual component rates (light) at  $\xi = 10$ . For  $\gamma = 5/3$ , the orbital signal is fully buried in broadband turbulent noise. For  $\gamma = 4/3$ , a residual peak at  $2\Omega$  survives above the continuum. For  $\gamma = 1$ , coherent peaks appear at  $4\Omega$  and  $8\Omega$ , with no power at  $2\Omega$ : the accretion rate responds nonlinearly to the quadrupolar forcing, transferring power to overtones. An observer would infer half the true orbital period.

Binary Bondi accretion provides a third route. The rotating quadrupolar potential drives shocks that generate entropy without viscosity, magnetic fields, or angular momentum in the ambient medium. The resulting flow shares the essential features of CDAFs – entropy-driven convection opposing infall, convective recycling, and suppression of  $\dot{M}$  – but the energy source is the orbital rotational energy rather than ‘viscous’ dissipation of the gas rotational energy. A related phenomenon appears in circumbinary disks, where [G. Ryan & A. MacFadyen \(2017\)](#) showed that tidally excited spiral shocks provide an effective viscosity  $\alpha \sim 0.01$  through purely hydrodynamic dissipation.

The suppression of  $\eta$  below unity reflects convective recycling rather than unbound mass loss: the turbulent interior circulates gas through large-scale eddies, and the accretion proceeds as a small net residual of nearly canceling inflow and outflow motions (Section 4.2). Whether a fraction of this recycled gas ultimately escapes to infinity with positive Bernoulli parameter – as in the ADIOS picture ([R. D. Blandford & M. C. Begelman 1999](#)) – is not determined by the present simulations, which maintain a fixed mass supply at the outer boundary.

The spectral distinction between the  $k^{-7/2}$  slope found here and the  $k^{-5/3}$  Kolmogorov scaling expected for vortical turbulence is a testable prediction for future MHD simulations.

## 5.2. Where Are the Periodic Binaries?

Searches for sub-parsec SMBH binaries have targeted periodic signatures in AGN light curves ([M. J. Graham et al. 2015](#); [M. Charisi et al. 2016](#); [T. Liu et al. 2019](#)), motivated by circumbinary disk simulations predicting periodic accretion modulation (e.g., [A. I. MacFadyen & M. Milosavljević 2008](#); [D. J. D’Orazio et al. 2013](#); [P. C. Duffell et al. 2020](#)). The yield has been disappointing: [T. Liu et al. \(2019\)](#) found most Pan-STARRS1 candidates did not persist, [S. Vaughan et al. \(2016\)](#) argued PG 1302–102 is consistent with red noise, and [K. El-Badry et al. \(2025\)](#) showed that all 181 Gaia DR3 periodic AGN candidates were false positives.

Our results offer a natural explanation. In radiatively inefficient environments ( $t_{\text{cool}} \gg NT$ ), the entropy instability drives turbulence that partially ( $\gamma = 4/3$ ) or fully ( $\gamma = 5/3$ ) buries the orbital signal in broadband noise (Section 4.4). In radiatively efficient environments ( $t_{\text{cool}} \ll NT$ ), the binary does produce coherent periodicity – but at  $4\Omega$  and  $8\Omega$ , not at the expected  $2\Omega$ . The accretion rate responds nonlinearly to the quadrupolar forcing, transferring power to overtones. An observer

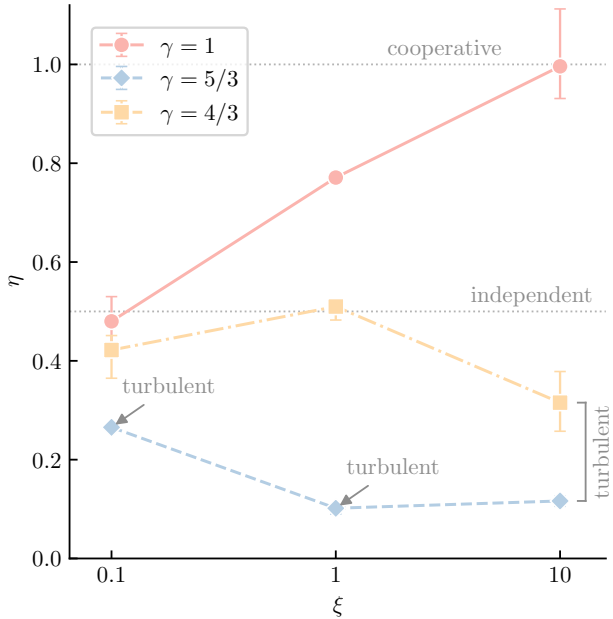


**Figure 7.** Accretion efficiency  $\eta \equiv \dot{M}_{\text{binary}}/\dot{M}_{\text{Bondi}}$  versus compactness  $\xi$  for equal-mass binaries at three adiabatic indices. The colors and line styles are the same as in Figure 5. Error bars span the 10th–90th percentile of  $\eta(t)$  measured over 5-orbit windows after  $t > t_B$ . Isothermal gas ( $\gamma = 1$ ) rises monotonically to  $\eta \rightarrow 1$ : the binary accretes cooperatively through a high-density bridge. Relativistic gas ( $\gamma = 4/3$ ) tracks the independent rate ( $\eta = 1/2$ ) at low  $\xi$ , then drops sharply once the sonic surface encloses the binary ( $\xi_m = 4$ ), as shock-generated entropy drives convective turbulence. Monatomic gas ( $\gamma = 5/3$ ) is turbulent and suppressed at all  $\xi$ . Dotted lines mark the cooperative ( $\eta = 1$ ) and independent ( $\eta = 1/2$ ) limits.

who found the  $4\Omega$  peak would infer half the true orbital period. The periodicity channel is not closed, but it is tuned to an unexpected frequency.

Three observational implications follow. First, the absence of periodicity at  $2\Omega$  does not exclude a binary: adiabatic binaries erase the signal, and isothermal binaries shift it. Second, the ratio of power at  $2\Omega$  to  $4\Omega$  encodes the mass ratio: for  $q = 1$  the half-orbit symmetry suppresses  $2\Omega$  in the total accretion rate. Third, kinematic signatures such as Doppler boosting of relativistic jets (S. O’Neill et al. 2022; S. Kiehlmann et al. 2025) bypass the accretion flow entirely and are unaffected by either the entropy instability or the nonlinear frequency shift. These remain the most robust electromagnetic probe of embedded binaries.

### 5.3. Astrophysical Applications

The single comparison  $t_{\text{cool}}$  versus  $NT$  partitions astrophysical binaries into three regimes. The thermodynamic regime – adiabatic, marginal, or isothermal –

depends on the cooling time at  $r \sim a$ , set by local microphysics (density, temperature, opacity), and is insensitive to the global flow geometry. The predicted efficiency  $\eta$ , by contrast, is calibrated to the spherical Bondi geometry simulated here and applies directly only when the flow at  $r \sim a$  is pressure-supported rather than rotationally supported.

#### 5.3.1. Adiabatic regime: $t_{\text{cool}} \gg NT$

Hot, radiatively inefficient environments place binaries in the adiabatic regime. Post-merger galaxies hosting SMBH binaries in tenuous plasma at temperature  $\Theta \sim 10^7$  K, and compact object binaries orbiting inside common stellar envelopes at  $\Theta \sim 10^5$  K, both satisfy  $t_{\text{cool}}/NT \gg 1$  across a wide range of separations and masses. In both cases the entropy instability is active, suppressing accretion to  $\eta \sim \mathcal{O}(0.1)$ . For SMBH binaries, laminar Bondi-based estimates of gas hardening adopted in population synthesis models (Z. Haiman et al. 2009; A. Sesana 2013; L. Z. Kelley et al. 2017) overestimate the hardening rate by  $1/\eta \sim 3$ –10, providing a thermodynamic ingredient in the final parsec problem (M. C. Begelman et al. 1980; M. Milosavljević & D. Merritt 2003) that is independent of feedback. For common envelope systems, Bondi–Hoyle–Lyttleton prescriptions used in single-body drag estimates (M. MacLeod & E. Ramirez-Ruiz 2015; M. MacLeod et al. 2017; S. De et al. 2020) do not capture the entropy feedback from the binary’s orbital motion and likely overestimate the accretion rate onto the embedded pair.

In both cases the principal caveat is geometry: the giant envelope has a steep density gradient and the SMBH environment may carry significant angular momentum, both of which violate the uniform pressure-supported medium assumed here. The thermodynamic regime ( $t_{\text{cool}}/NT \gg 1$ ) is robust because it depends only on local microphysics at  $r \sim a$ , but the quantitative  $\eta$  should be taken as indicative.

#### 5.3.2. Marginal regime: $t_{\text{cool}} \sim NT$

Dense, optically thick environments such as AGN disks place binaries near marginal cooling (I. Bartos et al. 2017; N. C. Stone et al. 2017; H. Tagawa et al. 2020). The thermodynamic outcome is sensitive to local conditions and the quantitative  $\eta$  from our spherical simulations does not apply directly: the disk scale height is comparable to or smaller than  $R_B$ , Keplerian shear introduces a velocity gradient across the Hill sphere, and residual angular momentum produces a circumbinary mini-disk. In the rotationally supported limit the propeller Mach number vanishes and the entropy instability is inoperative; a distinct suppression mechanism

driven by the narrowing of accretion streams operates instead (C. Tiede et al. 2025).

### 5.3.3. Isothermal regime: $t_{\text{cool}} \ll NT$

Efficiently cooled environments – molecular clouds, atomic cooling halos, and globular cluster gas – place binaries in the isothermal regime regardless of their microscopic  $\gamma$ . Post-shock entropy is radiated before the binary completes a single orbit, and the gas behaves as effectively isothermal. Binaries in these environments accrete cooperatively through a high-density bridge, with  $\eta \rightarrow 1$  and mass growth rates approaching twice the independent-accretor value. These systems are efficient accretors but poor periodic sources: the isothermal flow concentrates orbital power into overtones at  $4\Omega$  and  $8\Omega$  rather than  $2\Omega$  (Section 4.4), and kinematic signatures such as Doppler boosting (S. O’Neill et al. 2022) remain the most robust electromagnetic probe.

### 5.4. The Role of Cooling

Our simulations treat two limits:  $\gamma = 1$  (instantaneous cooling) and  $\gamma > 1$  (no cooling). The transition is sharp because the breakout number  $N$  is only  $\mathcal{O}(1)$ – $\mathcal{O}(10)$ : a system either cools faster than  $NT$  or it does not. When the cooling luminosity approaches  $L_{\text{Edd}}$ , radiation pressure stiffens the effective equation of state toward  $\gamma = 4/3$  – precisely the regime where the entropy instability is most potent. Eddington-limited accretion onto a single object proceeds unimpeded; onto a binary, it triggers the instability.

C. Tiede & D. J. D’Orazio (2025) reach a consistent conclusion from the spectral energy distribution (SED) side: only emission mechanisms with cooling times shorter than  $T$  carry orbital-period variability, while slower channels are damped. Our simulations provide the hydrodynamic mechanism: entropy-driven convection scrambles the accretion modulation before it imprints on the luminosity.

### 5.5. Caveats

The orbit is held fixed; for widely separated systems the inspiral timescale vastly exceeds the breakout timescale, so the steady state is established before the separation changes appreciably. We consider only  $q = 1$ ; for  $q \ll 1$  the entropy source weakens as  $q/(1+q)^2$  and the disruption timescale increases, though the container condition  $\xi > \xi_m$  is unchanged. Magnetic fields are absent; MHD effects could stabilize (tension) or enhance (magneto-rotational instability) the turbulence, and the spectral prediction  $k^{-7/2}$  versus  $k^{-5/3}$  provides a diagnostic. More generally, hotter environments that

most favor the entropy instability thermodynamically ( $\gamma_{\text{eff}}$  further from unity) also shrink the Bondi radius, reducing  $\xi$  and potentially moving the system out of the deeply embedded regime. This  $T$ – $\xi$  anticorrelation is a natural self-regulation: the conditions that make the instability most potent are also the conditions where embedding is hardest to achieve. The ambient medium is at rest and carries no angular momentum; a nonzero bulk velocity introduces BHL effects (R. Edgar 2004; A. Antoni et al. 2019), and residual rotation would produce a circumbinary structure whose interaction with the entropy instability is unexplored.

## 6. CONCLUDING REMARKS

A binary embedded in adiabatic gas generates the entropy that throttles its own accretion. The threshold  $\xi_m = 4/(5 - 3\gamma)$  – where  $\xi \equiv R_B/a$  is the dimensionless number characterizing the total Bondi radius,  $R_B$ , of the binary relative to the binary separation,  $a$  – and the breakout timescale  $N \propto (\gamma - 1)^{-1}\sqrt{\xi}$  – the number of orbits required to annihilate the Bondi saddle point and disrupt the transonic accretion flow – are derived from first principles; three-dimensional simulations confirm both. Embedded binaries in hot, radiatively inefficient environments are poor accretors (i.e., the ratio of the binary accretion rate relative to the accretion rate of a single body of equal mass,  $\eta \ll 1$ ) and poor periodic sources: gas-assisted hardening estimates for SMBH binaries in hot atmospheres that adopt laminar Bondi rates will overpredict the hardening rate by  $1/\eta \sim 3$ –10. Binaries in efficiently cooled environments accrete cooperatively and are undetectable through accretion-rate variability; kinematic signatures such as Doppler boosting remain viable. The dividing line is  $t_{\text{cool}}$  versus  $NT$ : systems that cool faster than they heat remain organized; systems that do not, go turbulent. This single comparison governs whether an embedded binary grows, stalls, or destroys its own fuel supply.

## ACKNOWLEDGEMENTS

M.D. thanks Jenny Greene, Jonathan Zrake, Andrei Gruzinov, Andrew MacFadyen, Ilya Mandel, Yacine Ali-Haïmoud, Romain Teyssier, Jeremy Goodman, Tamar Faran, Yuri Levin, and Philip Jon Østergaard Kirekberg for very fruitful discussions surrounding this problem.

*Software:* `matplotlib` (J. D. Hunter 2007), `cmasher` (E. van der Velden 2020), `SIMBI` (M. DuPont 2023), `numpy` (C. R. Harris et al. 2020), `scipy` (P. Virtanen et al. 2020)

## REFERENCES

- Acernese, F., Agathos, M., Agatsuma, K., et al. 2015, *Classical and Quantum Gravity*, 32, 024001, doi: [10.1088/0264-9381/32/2/024001](https://doi.org/10.1088/0264-9381/32/2/024001)
- Agazie, G., Anumalapudi, A., Archibald, A. M., et al. 2023, *ApJL*, 951, L8, doi: [10.3847/2041-8213/acdac6](https://doi.org/10.3847/2041-8213/acdac6)
- Antoni, A., MacLeod, M., & Ramirez-Ruiz, E. 2019, *ApJ*, 884, 22, doi: [10.3847/1538-4357/ab3466](https://doi.org/10.3847/1538-4357/ab3466)
- Artymowicz, P., & Lubow, S. H. 1994, *ApJ*, 421, 651, doi: [10.1086/173679](https://doi.org/10.1086/173679)
- Artymowicz, P., & Lubow, S. H. 1996, *ApJL*, 467, L77, doi: [10.1086/310200](https://doi.org/10.1086/310200)
- Bartos, I., Kocsis, B., Haiman, Z., & Márka, S. 2017, *ApJ*, 835, 165, doi: [10.3847/1538-4357/835/2/165](https://doi.org/10.3847/1538-4357/835/2/165)
- Begelman, M. C., Blandford, R. D., & Rees, M. J. 1980, *Nature*, 287, 307, doi: [10.1038/287307a0](https://doi.org/10.1038/287307a0)
- Berger, M. J., & Colella, P. 1989, *Journal of Computational Physics*, 82, 64, doi: [10.1016/0021-9991\(89\)90035-1](https://doi.org/10.1016/0021-9991(89)90035-1)
- Blandford, R. D., & Begelman, M. C. 1999, *MNRAS*, 303, L1, doi: [10.1046/j.1365-8711.1999.02358.x](https://doi.org/10.1046/j.1365-8711.1999.02358.x)
- Bondi, H. 1952, *MNRAS*, 112, 195, doi: [10.1093/mnras/112.2.195](https://doi.org/10.1093/mnras/112.2.195)
- Charisi, M., Bartos, I., Haiman, Z., et al. 2016, *MNRAS*, 463, 2145, doi: [10.1093/mnras/stw1838](https://doi.org/10.1093/mnras/stw1838)
- Cho, H., Prather, B. S., Narayan, R., et al. 2023, *ApJL*, 959, L22, doi: [10.3847/2041-8213/ad1048](https://doi.org/10.3847/2041-8213/ad1048)
- Colpi, M., Danzmann, K., Hewitson, M., et al. 2024, *arXiv e-prints*, arXiv:2402.07571, doi: [10.48550/arXiv.2402.07571](https://doi.org/10.48550/arXiv.2402.07571)
- De, S., MacLeod, M., Everson, R. W., et al. 2020, *ApJ*, 897, 130, doi: [10.3847/1538-4357/ab9ac6](https://doi.org/10.3847/1538-4357/ab9ac6)
- D’Orazio, D. J., Haiman, Z., & MacFadyen, A. 2013, *MNRAS*, 436, 2997, doi: [10.1093/mnras/stt1787](https://doi.org/10.1093/mnras/stt1787)
- Duffell, P. C., D’Orazio, D., Derdzinski, A., et al. 2020, *ApJ*, 901, 25, doi: [10.3847/1538-4357/abab95](https://doi.org/10.3847/1538-4357/abab95)
- DuPont, M. 2023, *SIMBI: 3D relativistic gas dynamics code*, *Astrophysics Source Code Library*, record ascl:2308.003 <http://ascl.net/2308.003>
- Edgar, R. 2004, *NewAR*, 48, 843, doi: [10.1016/j.newar.2004.06.001](https://doi.org/10.1016/j.newar.2004.06.001)
- Einfeldt, B. 1988, *SIAM Journal on Numerical Analysis*, 25, 294, doi: [10.1137/0725021](https://doi.org/10.1137/0725021)
- El-Badry, K., Hogg, D. W., & Rix, H.-W. 2025, *arXiv e-prints*, arXiv:2509.10601, doi: [10.48550/arXiv.2509.10601](https://doi.org/10.48550/arXiv.2509.10601)
- EPTA Collaboration, InPTA Collaboration, Antoniadis, J., et al. 2023, *A&A*, 678, A50, doi: [10.1051/0004-6361/202346844](https://doi.org/10.1051/0004-6361/202346844)
- Farris, B. D., Liu, Y. T., & Shapiro, S. L. 2010, *PhRvD*, 81, 084008, doi: [10.1103/PhysRevD.81.084008](https://doi.org/10.1103/PhysRevD.81.084008)
- Foglizzo, T., & Ruffert, M. 1997, *A&A*, 320, 342, doi: [10.48550/arXiv.astro-ph/9604160](https://doi.org/10.48550/arXiv.astro-ph/9604160)
- Graham, M. J., Djorgovski, S. G., Stern, D., et al. 2015, *Nature*, 518, 74, doi: [10.1038/nature14143](https://doi.org/10.1038/nature14143)
- Guo, M., Stone, J. M., Kim, C.-G., & Quataert, E. 2023, *ApJ*, 946, 26, doi: [10.3847/1538-4357/acb81e](https://doi.org/10.3847/1538-4357/acb81e)
- Guo, M., Stone, J. M., Quataert, E., & Springel, V. 2025, *ApJ*, 987, 202, doi: [10.3847/1538-4357/add1da](https://doi.org/10.3847/1538-4357/add1da)
- Haiman, Z., Kocsis, B., & Menou, K. 2009, *ApJ*, 700, 1952, doi: [10.1088/0004-637X/700/2/1952](https://doi.org/10.1088/0004-637X/700/2/1952)
- Harris, C. R., Millman, K. J., van der Walt, S. J., et al. 2020, *Nature*, 585, 357, doi: [10.1038/s41586-020-2649-2](https://doi.org/10.1038/s41586-020-2649-2)
- Harten, A., Lax, P. D., & Leer, B. v. 1983, *SIAM Review*, 25, 35, doi: [10.1137/1025002](https://doi.org/10.1137/1025002)
- Hunter, J. D. 2007, *Computing in Science & Engineering*, 9, 90, doi: [10.1109/MCSE.2007.55](https://doi.org/10.1109/MCSE.2007.55)
- Igumenshchev, I. V., & Abramowicz, M. A. 2000, *ApJS*, 130, 463, doi: [10.1086/317354](https://doi.org/10.1086/317354)
- Igumenshchev, I. V., & Narayan, R. 2002, *ApJ*, 566, 137, doi: [10.1086/338077](https://doi.org/10.1086/338077)
- Kagra Collaboration, Akutsu, T., Ando, M., et al. 2019, *Nature Astronomy*, 3, 35, doi: [10.1038/s41550-018-0658-y](https://doi.org/10.1038/s41550-018-0658-y)
- Kelley, L. Z., Blecha, L., & Hernquist, L. 2017, *MNRAS*, 464, 3131, doi: [10.1093/mnras/stw2452](https://doi.org/10.1093/mnras/stw2452)
- Kiehlmann, S., de la Parra, P. V., Sullivan, A. G., et al. 2025, *ApJ*, 985, 59, doi: [10.3847/1538-4357/adc567](https://doi.org/10.3847/1538-4357/adc567)
- Kim, H., & Kim, W.-T. 2007, *ApJ*, 665, 432, doi: [10.1086/519302](https://doi.org/10.1086/519302)
- Kim, H., Kim, W.-T., & Sánchez-Salcedo, F. J. 2008, *ApJL*, 679, L33, doi: [10.1086/589149](https://doi.org/10.1086/589149)
- Kim, W.-T. 2010, *ApJ*, 725, 1069, doi: [10.1088/0004-637X/725/1/1069](https://doi.org/10.1088/0004-637X/725/1/1069)
- Krumholz, M. R., McKee, C. F., & Klein, R. I. 2004, *ApJ*, 611, 399, doi: [10.1086/421935](https://doi.org/10.1086/421935)
- Lai, D., & Muñoz, D. J. 2023, *ARA&A*, 61, 517, doi: [10.1146/annurev-astro-052622-022933](https://doi.org/10.1146/annurev-astro-052622-022933)
- Landau, L. D., & Lifshitz, E. M. 1959, *Course of Theoretical Physics, Vol. 6, Fluid Mechanics* (London: Pergamon Press)
- LIGO Scientific Collaboration, Aasi, J., Abbott, B. P., et al. 2015, *Classical and Quantum Gravity*, 32, 074001, doi: [10.1088/0264-9381/32/7/074001](https://doi.org/10.1088/0264-9381/32/7/074001)
- Liu, T., Gezari, S., Ayers, M., et al. 2019, *ApJ*, 884, 36, doi: [10.3847/1538-4357/ab40cb](https://doi.org/10.3847/1538-4357/ab40cb)
- MacFadyen, A. I., & Milosavljević, M. 2008, *ApJ*, 672, 83, doi: [10.1086/523869](https://doi.org/10.1086/523869)
- MacLeod, M., Macias, P., Ramirez-Ruiz, E., et al. 2017, *ApJ*, 835, 282, doi: [10.3847/1538-4357/835/2/282](https://doi.org/10.3847/1538-4357/835/2/282)

- MacLeod, M., & Ramirez-Ruiz, E. 2015, *ApJ*, 803, 41, doi: [10.1088/0004-637X/803/1/41](https://doi.org/10.1088/0004-637X/803/1/41)
- Milosavljević, M., & Merritt, D. 2003, *ApJ*, 596, 860, doi: [10.1086/378086](https://doi.org/10.1086/378086)
- Narayan, R., Igumenshchev, I. V., & Abramowicz, M. A. 2000, *ApJ*, 539, 798, doi: [10.1086/309268](https://doi.org/10.1086/309268)
- Narayan, R., & Yi, I. 1994, *ApJL*, 428, L13, doi: [10.1086/187381](https://doi.org/10.1086/187381)
- Narayan, R., & Yi, I. 1995, *ApJ*, 452, 710, doi: [10.1086/176343](https://doi.org/10.1086/176343)
- O'Neill, D., D'Orazio, D. J., Samsing, J., & Pessah, M. E. 2024, *ApJ*, 974, 216, doi: [10.3847/1538-4357/ad7250](https://doi.org/10.3847/1538-4357/ad7250)
- O'Neill, S., Kiehlmann, S., Readhead, A. C. S., et al. 2022, *ApJL*, 926, L35, doi: [10.3847/2041-8213/ac504b](https://doi.org/10.3847/2041-8213/ac504b)
- Quataert, E., & Gruzinov, A. 2000, *ApJ*, 539, 809, doi: [10.1086/309267](https://doi.org/10.1086/309267)
- Reardon, D. J., Zic, A., Shannon, R. M., et al. 2023, *ApJL*, 951, L6, doi: [10.3847/2041-8213/acdd02](https://doi.org/10.3847/2041-8213/acdd02)
- Ressler, S. M., Combi, L., Ripperda, B., & Most, E. R. 2025, *ApJL*, 979, L24, doi: [10.3847/2041-8213/ad9eb5](https://doi.org/10.3847/2041-8213/ad9eb5)
- Ressler, S. M., Quataert, E., & Stone, J. M. 2020, *MNRAS*, 492, 3272, doi: [10.1093/mnras/stz3605](https://doi.org/10.1093/mnras/stz3605)
- Ruffert, M. 1994, *ApJ*, 427, 342, doi: [10.1086/174144](https://doi.org/10.1086/174144)
- Ryan, G., & MacFadyen, A. 2017, *ApJ*, 835, 199, doi: [10.3847/1538-4357/835/2/199](https://doi.org/10.3847/1538-4357/835/2/199)
- Sesana, A. 2013, *MNRAS*, 433, L1, doi: [10.1093/mnrasl/slt034](https://doi.org/10.1093/mnrasl/slt034)
- Stone, J. M., Pringle, J. E., & Begelman, M. C. 1999, *MNRAS*, 310, 1002, doi: [10.1046/j.1365-8711.1999.03024.x](https://doi.org/10.1046/j.1365-8711.1999.03024.x)
- Stone, N. C., Metzger, B. D., & Haiman, Z. 2017, *MNRAS*, 464, 946, doi: [10.1093/mnras/stw2260](https://doi.org/10.1093/mnras/stw2260)
- Tagawa, H., Haiman, Z., & Kocsis, B. 2020, *ApJ*, 898, 25, doi: [10.3847/1538-4357/ab9b8c](https://doi.org/10.3847/1538-4357/ab9b8c)
- Tiede, C., & D'Orazio, D. J. 2025, *ApJ*, 995, 68, doi: [10.3847/1538-4357/ae17ba](https://doi.org/10.3847/1538-4357/ae17ba)
- Tiede, C., Zrake, J., MacFadyen, A., & Haiman, Z. 2025, *ApJ*, 984, 144, doi: [10.3847/1538-4357/adc727](https://doi.org/10.3847/1538-4357/adc727)
- van der Velden, E. 2020, *The Journal of Open Source Software*, 5, 2004, doi: [10.21105/joss.02004](https://doi.org/10.21105/joss.02004)
- Vaughan, S., Uttley, P., Markowitz, A. G., et al. 2016, *MNRAS*, 461, 3145, doi: [10.1093/mnras/stw1412](https://doi.org/10.1093/mnras/stw1412)
- Virtanen, P., Gommers, R., Oliphant, T. E., et al. 2020, *Nature Methods*, 17, 261, doi: [10.1038/s41592-019-0686-2](https://doi.org/10.1038/s41592-019-0686-2)
- Xu, H., Chen, S., Guo, Y., et al. 2023, *Research in Astronomy and Astrophysics*, 23, 075024, doi: [10.1088/1674-4527/acdfa5](https://doi.org/10.1088/1674-4527/acdfa5)
- Zel'dovich, Y. B., & Raizer, Y. P. 1966, *Physics of Shock Waves and High-Temperature Hydrodynamic Phenomena*, ed. W. D. Hayes & R. F. Probstein, Vol. 1 (New York: Academic Press)